RESEARCH ARTICLE

Acoustic Tomography of Temperature Field by Finite Element Method and Improved Singular Value Decomposition-Based Tikhonov Regularization

HAITAO ZHANG[1,2], **QIANG LI**[1], **AND LIMING WANG**[1]

[1]National Key Laboratory of Information Detection and Processing, North University of China, Taiyuan 030051, China
[2]College of Information Engineering, Shanxi Vocational University of Engineering Science and Technology, Jinzhong 030619, China

Corresponding author: Liming Wang (wlm@nuc.edu.cn)

ABSTRACT The reconstruction algorithms play an important role in acoustic thermometry and are a research hotspot. This paper proposes a novel reconstruction method to improve the accuracy of temperature field reconstruction methods based on acoustic tomography. First, three mesh models are constructed by using the finite element method, which overcomes the defects of oversimplified classical discretization models. Secondly, the coefficient matrix A of the acoustic thermometry forward problem is calculated offline, and then the temperature values of several points in the measurement are obtained by solving the inverse problem using the improved regularization method based on singular value decomposition. Finally, the temperature profile of the entire region is obtained through interpolation. The correctness and feasibility of the proposed method are validated through simulations and experimental testing with three different temperature fields. Results show that the proposed method has satisfactory reconstruction accuracy and provides a different solution for reconstructing the ultrasound temperature field.

INDEX TERMS Acoustic tomography, temperature field, finite element, singular value decomposition, regularization, interpolation.

I. INTRODUCTION

The acoustic tomography temperature field reconstruction technique calculates the temperature distribution of the measured area based on the time of flight (TOF) of sound waves between the transceivers around the measured area. Because of its advantages of a non-contact and non-destructive temperature field, a wide range of temperature measurements, and strong adaptability to the environment, it has become a research hotspot in the field of temperature field measurements. Monitoring the temperature profile of industrial boilers is a typical application of this technique. Meanwhile, researchers are using this technique to monitor temperature profiles in deep-sea hydrothermal vents, the atmosphere,

The associate editor coordinating the review of this manuscript and approving it for publication was Arturo Conde.

stored grains, and stacked materials. Most research has focused on a few factors, such as the composition of the measured medium, the measurement accuracy of the TOF of acoustic waves, the reconstruction algorithm of the temperature field, the layout of acoustic transducers [1], as well as the bending effect of the acoustic propagation path [2]. Various reconstruction algorithms have been proposed to improve reconstruction accuracy [3], [4], [5], [6].

Common reconstruction methods can be divided into two categories. One is the discrete region method. The classical methods for ultrasonic temperature field reconstruction require discretization of the reconstructed regions, each of which is referred to as a grid or pixel. The velocity in the grid and the distance traversed by the sound ray are employed to model the forward problem $Ax=t$, where A represents the distance coefficient matrix, x denotes the slowness

(the inverse of the velocity), and *t* denotes the TOF vector. The temperature value in each grid is assumed to be the average temperature of the grid, which is a constant. Then, the continuous temperature field can be obtained by using the interpolation method. This is the most common method used in acoustic temperature field reconstruction, but it has two drawbacks. One is that the temperature in the grid is simply regarded as a constant, which reduces the model's accuracy and increases the reconstruction error. Another drawback is that the temperature field needs to be reconstructed by interpolation, and the geometric center of the grid is often chosen as the interpolation point, leading to the failure to obtain the temperature field outside the interpolation point, i.e., the temperature distribution at the edge of the measured area cannot be obtained.

Another category of common reconstruction methods is the series expansion method. In such methods, the parameter field is approximated with an expansion of a continuous function consisting of a set of basis functions and unknown coefficients. Different from the first category, considering the continuity of the function, the prior information of continuity is incorporated into the reconstruction of the temperature field, which guarantees the smoothness of the temperature field and reduces the ill-condition of the problem. By solving the coefficient of this function, the parameter distribution can be reconstructed. However, it is difficult to obtain a satisfactory temperature field by this method. Also, when using the method, the following problems need to be solved, such as the selection of shape parameters, the types of basis functions, and the collocation of basis function central points, which affect the improvement of reconstruction accuracy. Besides, since the method adopts the idea of global approximation, the reconstructed temperature field is too smooth to well display the details of the temperature field.

In this paper, the finite element method is adopted to construct three mesh models, and the accuracy of modeling is improved by approximating the internal slowness of the mesh using a linear combination of the values of the slowness at the nodes of the mesh, thereby overcoming the shortcomings of oversimplified classical discretization models. Additionally, the local details of the temperature field are improved by using the method of piecewise function local approximation.

The ill-posed problem needs to be solved by reconstruction algorithms after establishing the mathematical model of the temperature field. Currently, non-iterative methods and iterative methods are the two main reconstruction algorithms. Conventional non-iterative methods include the filter back projection (FBP), the linear back projection (LBP), the least squares method (LSM), and some kernel function approaches. As the conventional algorithms for reconstructing temperature distributions, FBP, LBP, and LSM have the advantages of low computational complexity and understandable principles. However, in these algorithms, the number of effective acoustic wave propagation routes needs to be larger than the number of divided grids, which limits resolution of the reconstructed images. For the reconstructed

temperature values of kernel function approaches, the transition information from the high-temperature region to the low-temperature region is not completely reconstructed, and the shape of the reconstructed isotherms is distorted.

Conventional iterative methods include the algebraic reconstruction technique (ART), the simultaneous iterative reconstruction technique (SIRT), and the Landweber iteration algorithm. These iterative algorithms exhibit better convergence and stability with lower reconstruction errors. However, they have longer computing time than noniterative algorithms. These iterative methods can be understood as optimization methods for weighted least squares problems. However, these algorithms may demonstrate varying numerical performances in different applications, which need to be further analyzed.

In recent years, many high-performance reconstruction algorithms have been proposed to continuously improve the reconstruction quality of acoustic tomography. Kolouri et al [7], [8] first showed the effectiveness of an unscented Kalman filter (UKF) for the non-linear travel time under specific measurement situations. They calculated the scalar and vector tomography of the atmosphere by using this inverse approach. Also, they pointed out that the computational complexity of the time-dependent stochastic inversion (TDSI) technique is significantly higher than that of the UKF approach. Moreover, Zhang et al. [9] evaluated the reconstruction performance of the covariance matrix adaptation evolution strategy (CMA-ES) algorithm. Niu et al. [10] utilized the Gaussian parametric level set method coupled with regularized Landwebe to reconstruct the temperature fields. This novel technique has proven to be very promising in reconstructing temperature in non-axisymmetric distribution. Niu et al. developed a combination technique based on the Kalman filter and the recursive least square estimator (KF-RLSE) to reconstruct the temperature fields [11]. High-precision reconstruction may also be generated by using the Legendre polynomial method, where the expansion coefficients could be considered as slowness and the polynomial functions will be employed to reconstruct the temperature.

Many deep learning-based reconstruction methods have been proposed to reconstruct the temperature field or velocity field. Kong et al. employed the radial basis function neural network (RBFNN) to measure the velocity field of the boiler and furnace [12]. A novel improved RBFNN acoustic algorithm was used to reconstruct two-dimensional velocity fields. Also, they considered adding adjustable linear polynomials in the RBF layer to enhance its performance. Zhang and Li proposed a two-stage algorithm based on virtual observation (VO) and residual network (ResNet) [13]. ResNet was constructed to predict the temperature distribution under the refined grid, and the dual-input model was utilized to enhance the network's generalization ability. Lin et al. designed a convolutional neural network (CNN) to train a machine-learning model that can reconstruct a gas temperature distribution from acoustic velocities [14]. By adjusting the label and the loss function, a practical training approach was

developed. The proposed neural networks can be considered a reliable and efficient 2-D gas temperature field reconstruction methodology.

In recent years, more reconstruction methods based on deep learning have been provided for under-determined inverse problems, indicating the main research direction of this field in the future. Wu et al. [15] proposed a wavelet-improved score-based generative model to alleviating inaccurate distribution of the data distribution gradient and enhancing the overall stability for medical imaging. The modal has demonstrated remarkable performance in addressing challenging under-determined inverse problems in medical imaging. Guo et al. [16] proposed an iterative deep reconstruction network to synergize unsupervised method and data priors into a unified framework. The method employs an unsupervised deep training strategy to obtain high-quality images from noisy data in an end-to-end fashion. Three large-scale preclinical datasets experiments demonstrate that the method reconstructs better image quality than other state-of-the-art methods. Wu et al. [17] proposed a deep embedding attention refinement (DEAR) network to address sparse-view tomography imaging. The results on clinical datasets demonstrate the efficiency of the proposed DEAR in edge preservation and feature recovery.

In this paper, an improved singular value decomposition (SVD)-based Tikhonov regularization method is proposed to handle ill-posed problems since the standard Tikhonov regularization method makes no difference correction to all singular values. The proposed method improves the generalized inverse operation method based on the principle of least squares. By regularizing adjustment, the singular matrix is replaced by a full-rank matrix, and then the ill-posed problem is transformed into a well-posed problem so that the ill-posed problem can obtain a unique solution.

The rest of the paper is organized as follows. In Section II, the temperature field reconstruction principle of acoustic tomography is introduced, the two common models are described, and the mathematical model of the forward problem is established. In Section III, the proposed finite element-based discretization model is presented. In Section IV, an improved Tikhonov regularization method is proposed for solving the inverse problem. In Section V, a qualitative and quantitative analysis is conducted by simulating several typical temperature fields, and the results demonstrate the effectiveness and robustness of the proposed method. In Section VI, an experiment system is constructed to verify the effectiveness of the proposed reconstruction algorithm. Finally, this paper is concluded in Section VII.

The main contributions of this paper are as follows.

1) Three mesh models based on the finite element method are proposed to formulate the forward problem for AT temperature field reconstruction.

2) Three types of discretization methods of temperature field are analyzed and compared, and their advantages and disadvantages are discussed. The proposed method is more computationally intensive but has higher accuracy.

3) The inverse problem is solved with the improved SVD-based Tikhonov regularization method.

4) A corresponding experimental platform is built to verify the correctness and effectiveness of the proposed method.

II. PRINCIPLE OF ACOUSTIC TOMOGRAPHY THERMOMETRY

The relation between the propagation velocity of acoustic waves in a gas medium and the thermodynamic absolute temperature of the gas medium is expressed in (1):

$$c = \sqrt{\frac{\gamma R}{M} T} = Z \sqrt{T}. \tag{1}$$

where c denotes the velocity of sound (m/s), γ denotes the ratio of specific heats (1.4 for air), R represents the ideal gas constant (8.314 J/mol·K), M represents the molar mass of gas (28.8×10^{-3} kg/mol), and T denotes the thermodynamic absolute temperature (K). If the gas medium is known, Z is a constant (20.045 for air). Therefore, the acoustic velocity in the gas medium can be considered a unary function of the temperature of the gas medium. To obtain the temperature distribution of the measured area, it should be divided into N grids (pixels), and several acoustic transceivers should be set around the measured area to form M effective acoustic paths. The sound propagation medium can be considered a homogeneous medium. When the sound velocity is relatively large or the temperature field gradient change in a high-temperature environment is small, the sound wave can be approximately regarded as propagating along a straight line. Figure 1 shows a typical layout of transducers and the effective acoustic paths between the transducers. The TOF of acoustic waves along the M effective paths can be obtained via measurements or simulations. Then, the acoustic velocity distribution in the measured area can be reconstructed by using the TOF and an appropriate reconstruction algorithm. Finally, temperature distribution can be obtained using (1).
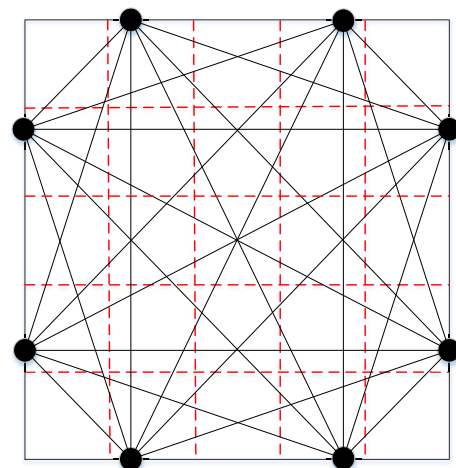

FIGURE 1. Transducer layouts and effective acoustic paths.

Assume that acoustic waves propagate along a straight line and any two acoustic sensors correspond to a ray. The time

consumed for its transmission is the TOF, which is a function of slowness and distance. Let the measured temperature field be $T(x, y)$ and the slowness distribution of acoustic waves be $f(x, y)$; then, the TOF t_k along any path l_k can be expressed in (2):

$$t_k = \int_{l_k} f(x, y) dl \quad k = 1, 2, \cdots, M. \tag{2}$$

where M denotes the number of effective acoustic paths. This paper introduces a classical description model for the forward problem. The measured temperature field is divided into N grids, the temperature in each grid is unknown and assumed to be uniform, and then the reconstruction requires finding the temperature in each grid. Equation (2) can be discretized as follows.

$$t_k = \sum_{i=1}^{N} \Delta A_{k,i} f_i \tag{3}$$

where t_k denotes the TOF of the sound wave along the k-th ray, $\Delta A_{k,i}$ denotes the distance of the k-th effective path going through the i-th grid, f_i represents the slowness within the i-th grid, and N represents the total number of grids.

Considering all M valid acoustic rays, (3) can be represented in a matrix form.

$$Ax = t \tag{4}$$

where $t = (t_1, t_2, \cdots, t_M)'$ denotes the m-dimensional column vector corresponding to the TOF of each ray. $x = (x_1, x_2, \cdots, x_N)'$ represents the slowness value in the discrete cell, and it is a n-dimensional column vector. A is a matrix of order M×N with corresponding elements $A_{i,j}$.

After discretization, the problem is transformed into solving a matrix equation. In this case, the matrix equation needs to be over-determined before it can be solved. However, there is one serious drawback in the above description, i.e., it is not reasonable to assume that the value of the slowness within each grid is a constant to be solved. The larger the grid, the larger the error introduced by the model.

The equation $Ax = t$ is ill-conditioned since small perturbations of vector t will lead to a significant change in the solution. Assuming that the observed data t has a minor perturbation δt, and the corresponding perturbation of the solution is δx, then the equation $Ax = t$ becomes:

$$A(x + \delta x) = t + \delta t.$$

Then,

$$\delta x = A^{-1} \delta t$$

where A^{-1} denotes the generalized inverse of matrix A. According to the property of subordinate norms, we have

$$\|\delta x\| = \left\| A^{-1} \delta t \right\| \leq \left\| A^{-1} \right\| \|\delta t\|$$

$$\|x\| \geq \frac{\|Ax\|}{\|A\|} = \frac{\|t\|}{A}.$$

Then,

$$\frac{\|\delta x\|}{\|x\|} \leq \frac{\left\| A^{-1} \right\| \|\delta t\|}{\|t\| / \|A\|}$$

Thus,

$$\frac{\|\delta x\|}{\|x\|} \leq cond(A) \frac{\|\delta t\|}{\|t\|}$$

where $cond(A)$ represents the condition number of matrix A, and it is a constant once the coefficient matrix A is determined. When the observed data t has minor measurement errors, the relative error of the solution is determined by the measurement error. In practical scenarios, t will inevitably contain measurement errors. Thus, a precise TOF measurement method is required to reduce the measurement error of t. To facilitate the discussion of our proposed reconstruction algorithm, the error of t is ignored in this paper.

The following introduces the reconstruction model based on radial basis functions [15], [16], [17]. The slowness is expressed as a linear combination of N-radial basis functions.

$$f(x, y) = \sum_{j=1}^{N} x_j \varphi_j \tag{5}$$

where x_j denotes the N undetermined coefficients, and φ_j represents the radial basis function whose center lies inside the temperature field.

Combining (2) and (5), we have

$$t_k = \sum_{j=1}^{N} a_{kj} x_j, \quad a_{kj} = \int_{l_k} \varphi_j dl_k. \tag{6}$$

Consider M sound rays and define

$$\begin{cases} A = (a_{kj})_{k=1,\cdots,M; j=1,\cdots,N} \\ x = (x_1, x_2, \cdots, x_N)' \\ t = (t_1, \cdots, t_M)' \end{cases}$$

Thus, Equation (6) can be represented in a matrix form

$$Ax = t \tag{7}$$

A in (4) and (7) can be obtained after the transducer position and grid are determined, and t can be obtained by simulation calculation or actual measurement. After obtaining the coefficient matrix A and the sound propagation time t, Equations (4) and (7) can be solved using various reconstruction algorithms. Though (7) and (4) are formally identical, they differ in the physical meaning of the quantities at the left end of the equation. In (4), A is the ray segment matrix, and the unknowns are the average temperature of each grid. In (7), A is the integral coefficient matrix obtained by integrating the basis functions, and the unknowns are the weighting coefficients corresponding to each basis function. The second model is better than the first one because it does not require the subsequent interpolation operation to obtain the temperature field $T(x, y)$, and there is no obvious defect in the model, so it has higher reconstruction accuracy. Researchers have conducted numerous studies around the radial basis function method.

III. FORWARD PROBLEM MODELING BASED ON THE FINITE ELEMENT METHOD

In Section II, it is shown that the acoustic temperature field reconstruction algorithm first establishes the mathematical model $Ax=t$ and then solves the inverse problem via various algorithms. To solve this problem, the temperature field needs to be discretized and divided into grids of a regular shape. Assuming that the internal and boundary slowness of each mesh can be represented by the slowness values assigned at the nodes of the mesh, some interpolation methods can be employed to find the values between nodes. In this approach, the drawback that the classical discretization model considers the grid temperature value as a constant can be overcome. The limiting case of infinitely many grids is equivalent to the case where the temperature field is smooth and continuous. In our algorithm, a grid model is applied where the unknown slowness $f(x, y)$ is approximated as a linear combination of the slowness values of the grid nodes.

$$f(x, y) = \sum_{k=1}^{N} f_k N_k(x, y) \tag{8}$$

where f_k denotes the slowness value of the node, N_k is an interpolation function (shape function). Generally, first- or second-order polynomials are utilized to interpolate the slowness values between nodes. For example, the measured area with triangles can be covered, where N=3, and the function $N_k(x, y)$ can be a two-dimensional first-order polynomial. The distribution of slowness for each triangle is approximated as a plane. This is a standard interpolation in finite element methods, which is known as the linear Lagrangian triangle interpolation. The space generated by nodal variables is a two-dimensional space of continuous piecewise linear functions. Equation (9) can be solved by considering the discretization and substituting (8) into (2).

$$t_\Gamma = \int_\Gamma f(x, y)\, dl = \sum_{j=1}^{J} \int_{\Gamma_j} f(x, y)\, dl$$

$$= \sum_{j=1}^{J} \int_{\Gamma_j} \sum_{k=1}^{3} f_k N_k(x, y)\, dl$$

$$= \sum_{j=1}^{J} \sum_{k=1}^{3} \left(\int_{\Gamma_j} N_k(x, y)\, dl \right) f_k \tag{9}$$

where J denotes the total number of triangle grids traversed by a ray, which can be regarded as the total number of triangle grids because the integral term is 0 for triangles that are not traversed by a ray. j denotes the index of the current triangle. $\Gamma_j = \Gamma \cap \Delta_j$ denotes the part of the sound ray that passes through the j-th triangle. The matrix form of (9) is

$$Ax = t. \tag{10}$$

where x represents the slowness value vector of all triangle nodes, and it is the parameter to be evaluated. t denotes the

TOF vector. Matrix A is called a piecewise integral summation coefficient matrix, and its element is $\int_{\Gamma_j} N_k(x, y)\, dl$. Matrix A reflects the linear relationship between the measurements and the unknowns, and it is different from the distance coefficient matrix in (4) and the integration coefficient matrix in (7). From the names of the three matrices, it can be seen that their solution processes are different. Here, this paper focuses on the solution of A in (10). The grid cells and nodes are illustrated in Figure 2.
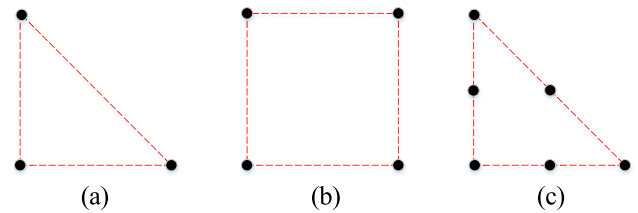

FIGURE 2. Grid cells and nodes. (a) 3-node cell. (b) 4-node cell. (c) 6-node cell.

Figure 2 demonstrates a 3-node triangular cell on the left, a 4-node square cell in the middle, and a 6-node triangular cell on the right. Based on the 3-node cell, the 6-node cell is formed by adding the midpoints of the three edges of the triangle as additional nodes. Taking the 3-node triangular cell as an example, the piecewise integral summation coefficient matrix A is solved, i.e., the integral term $\int_{\Gamma_j} N_k(x, y)\, dl$ in (9). After the transducer position and grid distribution are determined, the integration path is determined, and the problem can be transformed into solving the shape function $N_k(x, y)$. Taking the 3-node triangular cell as an example, the corresponding shape function is solved. As shown in Figure 3, the numbers of the three nodes are 1, 2, and 3, and their respective position coordinates are (x_i, y_i), $i = 1, 2, 3$. The slowness values of the three nodes are f_1, f_2, and f_3, respectively.
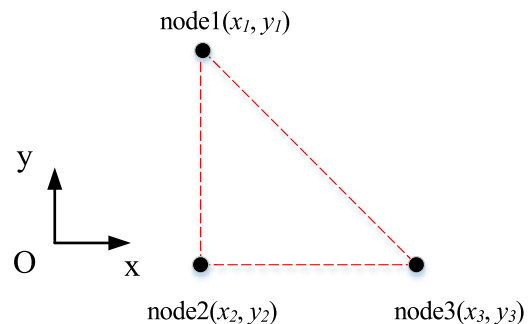

FIGURE 3. 3-node triangular cell.

The slowness of a triangular cell can be expressed by a two-dimensional first-order polynomial as follows

$$f(x, y) = c_1 + c_2 x + c_3 y \tag{11}$$

where c_1, c_2, and c_3 are the undetermined coefficients. Substituting the node coordinates into (11), the values of $c_1, c_2,$

and c_3 can be obtained.

$$\begin{bmatrix} f_1 \\ f_2 \\ f_3 \end{bmatrix} = \begin{bmatrix} 1 & x_1 & y_1 \\ 1 & x_2 & y_2 \\ 1 & x_3 & y_3 \end{bmatrix} \begin{bmatrix} c_1 \\ c_2 \\ c_3 \end{bmatrix} \Longrightarrow \begin{bmatrix} c_1 \\ c_2 \\ c_3 \end{bmatrix}$$
$$= \begin{bmatrix} 1 & x_1 & y_1 \\ 1 & x_2 & y_2 \\ 1 & x_3 & y_3 \end{bmatrix}^{-1} \begin{bmatrix} f_1 \\ f_2 \\ f_3 \end{bmatrix} \qquad (12)$$

Substituting (12) into (11) yields

$$f(x, y) = \begin{bmatrix} 1 & x & y \end{bmatrix} \begin{bmatrix} c_1 \\ c_2 \\ c_3 \end{bmatrix} = \begin{bmatrix} 1 & x & y \end{bmatrix} \begin{bmatrix} 1 & x_1 & y_1 \\ 1 & x_2 & y_2 \\ 1 & x_3 & y_3 \end{bmatrix}^{-1} \begin{bmatrix} f_1 \\ f_2 \\ f_3 \end{bmatrix}$$
$$= \begin{bmatrix} N_1(x, y) & N_2(x, y) & N_3(x, y) \end{bmatrix} \begin{bmatrix} f_1 \\ f_2 \\ f_3 \end{bmatrix}. \qquad (13)$$

where $N_1(x, y)$, $N_2(x, y)$, $N_3(x, y)$ are the shape function or interpolation function. The shape function depends only on the nodal coordinates and is independent of the nodal retardation value. After the shape function is solved, the coefficient matrix A can be obtained by solving the integral term in (9). Though the computational procedure is cumbersome and time-consuming, it can be conducted offline in advance.

The following introduces how to solve the shape function for a 4-node square cell and a 6-node triangular cell. Since there are four and six nodal values, there will be four and six undetermined coefficients. The slowness function requires quadratic terms in x and y, which also appear in the shape function. Based on (11), the slowness function of the 4-node cell and the 6-node cell can be obtained, as shown in (14) and (15).

$$f(x, y) = c_1 + c_2 x + c_3 y + c_4 xy \qquad (14)$$
$$f(x, y) = c_1 + c_2 x + c_3 y + c_4 x^2 + c_5 xy + c_6 y^2 \qquad (15)$$

The quadratic terms in x and y appear in (14) and (15). The derivation of the shape function follows the same procedure as that of the 3-node cell. The 4-node cell shape functions are $N_1(x, y)$, $N_2(x, y)$, $N_3(x, y)$, and $N_4(x, y)$. The 6-node cell shape functions are $N_1(x, y)$, $N_2(x, y)$, $N_3(x, y)$, $N_4(x, y)$, $N_5(x, y)$, and $N_6(x, y)$.

To sum up, once the shape function is obtained, the coefficient matrix A can be calculated, which describes the linear relationship between the known and unknown quantities (TOF and slowness). Different shape functions have different computational accuracies. Since the 4- and 6-node shape functions contain quadratic terms in x and y, the model has higher accuracy and better functional approximation capabilities, and the final temperature field is more accurate. However, the number of unknowns and the computational complexity rise steeply with the number of nodes, eventually leading to the problem of solving large underdetermined linear equations. This problem will be solved in the next section.

IV. THE METHOD FOR SOLVING THE INVERSE PROBLEM

For the classical discretization model method, the radial basis function global approximation method, or the polynomial piecewise approximation method proposed in this paper, the linear equations (4), (7), and (10) need to be solved to obtain the temperature distribution. Their general form is given below:

$$Ax = b. \qquad (16)$$

where A is a known matrix of order M×N; M denotes the number of equations, and it is determined by the number of effective rays; N denotes the number of desired unknowns, which can be slowness or weight coefficients, determined by the number of grids, basis functions, or nodes; b represents the TOF data, which can be obtained from real measurements or simulations. Here, x is an unknown quantity, and this is a classical inverse problem. Generally, inverse problems can be divided into two categories: solving equations where the number of unknowns is small compared to the number of equations, and solving equations where the number of unknowns is large. These two types of equations are referred to as overdetermined or underdetermined equations.

The least-squares method is a popular method for solving discrete models of classical forward problems. In this case, the number of rays needs to be larger than the number of grids, i.e., Equation (16) becomes an overdetermined system of equations. However, there are two problems with the least squares method. The first, as mentioned in Section II, is the low reconstruction accuracy due to imperfections in the discretization model. The second is the impossibility of reconstructing the temperature field outside the sampling points since the interpolation method is employed to obtain a finer temperature field distribution after obtaining the temperature values at the geometrical center of the grid. Since the accuracy is not high, extrapolation is not used, and only the temperature field inside the sampling point can be reconstructed. In practical applications, due to various external constraints and cost reduction considerations, it is not desirable to install too many transducers, causing the number of sound rays smaller than the number of unknowns, and in this case, Equation (16) becomes an underdetermined system of equations. Researchers have mainly focused on solving underdetermined equations, which are more practical, but underdetermined problems can lead to ill-posed and ill-conditioned solutions. Specifically, ill-posedness implies that the solution of equations is unstable and not unique, and ill-conditioning implies that a small perturbation in the measurement data b will cause a drastic shift in the solution of an equation. Therefore, it is necessary to adopt a suitable reconstruction algorithm that can avoid the above problems and reconstruct the temperature field more accurately.

The methods for solving underdetermined systems of equations can be mainly divided into two categories: SVD-based regularization methods [18], [19], and various optimization methods. The general idea behind most inversion

methods is to solve the following minimization problem.

$$\min \|Ax - b\|_2^2 \qquad (17)$$

The minimization problem can be formulated as follows

$$A^T Ax = A^T b \qquad (18)$$

After applying SVD to matrix A, the least squares solution of (16) can be expressed as follows.

$$x = \sum_{i=1}^{p} \frac{u_i^T b}{\sigma_i} v_i \qquad (19)$$

where $\sigma_1 \geq \sigma_2 \geq \cdots \geq \sigma_p > 0$ is the singular value of the matrix, p denotes the total number of nonzero singular values, and u_i and v_i represent the left and right singular vectors of matrix A, respectively. Due to the ill-posedness of the inverse problem, the condition number will be large, which will lead to very small singular values. According to (19), if σ_i is small, the small measurement error of b will be magnified many times, and the solution will deviate seriously from the true solution. Based on SVD, Tikhonov regularization is employed to suppress the error of the solution. The basic idea is to incorporate prior information about the solution into the original problem to minimize a certain norm of the solution while ensuring the fit of the data. Considering the solution of the inverse acoustic CT problem, i.e., the sound velocity value is a bounded positive number, the following minimization problem is solved:

$$\min \|Ax - b\|_2^2 + \mu \|x\|_2^2. \qquad (20)$$

The minimization problem can be formulated as (21).

$$(A^T A + \mu I)x = A^T b \qquad (21)$$

where $\mu > 0$ is the regularization parameter, and I is the identity matrix. The solution of (21) is represented in (22).

$$x = \sum_{i=1}^{p} \frac{\sigma_i^2}{\sigma_i^2 + \mu} \frac{u_i^T b}{\sigma_i} v_i = \sum_{i=1}^{p} \frac{u_i^T b}{\sigma_i + \mu/\sigma_i} v_i \qquad (22)$$

where $f = \frac{\sigma_i^2}{\sigma_i^2 + \mu}$ is the filtering factor. According to (18) and (21), Tikhonov regularization does not directly transform matrix A but transforms the normal equation $A^T Ax = A^T b$ of the original equation $Ax = b$ by replacing the ill-conditioned matrix $A^T A$ with a well-conditioned matrix $A^T A + \mu I$, and then transforms the ill-posed problem into a well-posed problem.

In this paper, an improved Tikhonov regularization method is developed to solve the inverse problem. The standard Tikhonov regularization method makes no difference correction to all singular values. In practice, a more reasonable correction method is that the larger the singular value, the smaller the correction amplitude, and vice versa. Firstly, by using the threshold singular value σ_t, the singular values are divided into large singular values and small singular values, where the ones are not modified while the small ones need to be corrected, and the smaller the singular value,

the greater the correction amplitude. In this paper, the minimum singular value satisfying (23) is set as the threshold singular σ_t.

$$\sigma_t \geq \max_{1 \leq j \leq p} k\sigma_j \qquad (23)$$

where k is the threshold obtained by experience.

The filtering factors of improved Tikhonov regularization are given below:

$$f = \begin{cases} 1, & 1 < i < 0 \\ \sigma_i^2 \left[\sigma_i^2 + \mu \left(\frac{\sigma_t}{\sigma_i} \right)^{1/2} \right]^{-1}, & t \leq i \leq p \end{cases} \qquad (24)$$

V. NUMERICAL CALCULATION AND SIMULATION EXPERIMENT
A. BUILDING SIMULATION MODEL
To verify the correctness and validity of the model presented in Section III, several temperature fields are simulated using the reconstruction algorithm in Section IV, and the constructed simulated model is illustrated in Figure 4. The measured area is a square area of 12×12. The locations of the eight ultrasound transducers are known, and they are uniformly placed on the four edges to form 24 effective acoustic paths. The measured area is divided into 25 square grids, and each grid is divided into two isosceles right triangles. Figure 4(a) and (b) correspond to triangular cells, while Figure 4(c) corresponds to square cells. It can be seen that the difference between Figure 4(a) and (b) is the triangulation of the four corners. After performing numerical calculations beforehand and referring to existing studies, it was found that the four corner nodes had large computational errors and thus were discarded. The reason is that very few rays pass through the triangle where the four nodes are located, so the nodes are used fewer times in the calculation. Similarly, the square cells with four corners are replaced by four triangular cells in Figure 4(c). Therefore, there are 32 slowness values to evaluate for both the 3-node triangular and square models, while there are 109 slowness values for the 6-node triangular model. After the slowness values are obtained, the two-dimensional piecewise function of the temperature distribution can be obtained by (1) and (13), or the distribution of the temperature field can be obtained by interpolation.
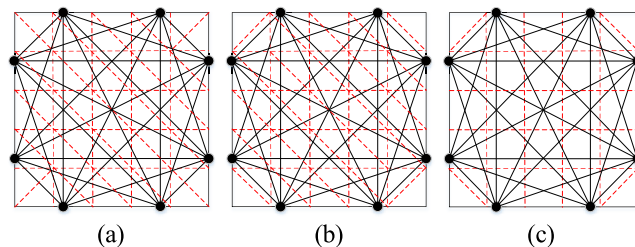

FIGURE 4. Different cell models. (a) Complete triangle model. (b) Incomplete triangle model. (c) Square model.

Different cell models in Figure 4 are used to simulate and reconstruct the temperature field in three distributions:

unimodal symmetric, unimodal skew, and bimodal skew. The initial temperature field model is presented in Figure 5. The temperature field is given in (25), (26), and (27).

The unimodal symmetry model is represented as:

$$T(x, y) = 800 \sin\left(\frac{\pi x}{12}\right) \sin\left(\frac{\pi y}{12}\right) + 1200 \quad (25)$$

The unimodal skew model is represented as:

$$T(x, y) = 1200 \exp\left[-\frac{(x-8)^2 + (y-4)^2}{100}\right] + 800 \quad (26)$$

The bimodal skew model is represented as:

$$T(x, y) = 1200 + 800 \exp\left[-0.2(x-3.5)^2 - 0.06(y-7)^2\right] + 600 \exp\left[-0.2(x-9)^2 - 0.04(y-4.5)^2\right] \quad (27)$$
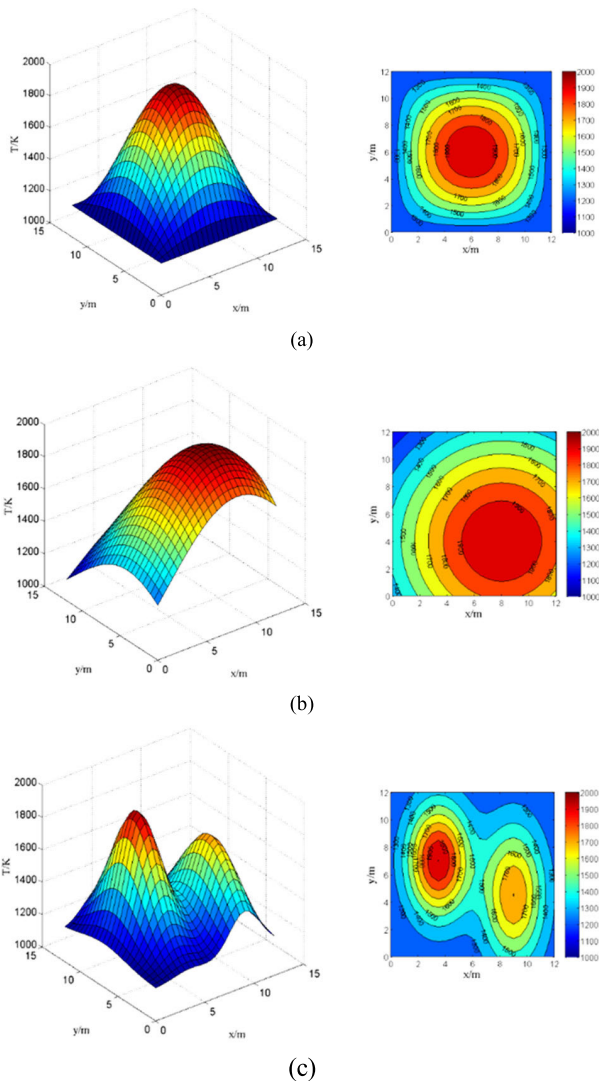

(a)

(b)

(c)

FIGURE 5. Temperature field models. (a) unimodal symmetry model. (b) unimodal skew model. (c) bimodal skew model.

B. SIMULATION RESULTS AND DATA ANALYSIS

The quality of the reconstructed temperature field can be evaluated based on the maximum relative error E_{max}, the average relative error E_{ave}, and the root mean square error E_{rms}. They are defined as follows:

$$E_{max} = max \left| \frac{\hat{T}(i) - T(i)}{T(i)} \right| \times 100\%, i = 1, 2, \cdots, M \quad (28)$$

$$E_{ave} = \frac{1}{M} \sum_{i=1}^{M} \left| \frac{\hat{T}(i) - T(i)}{T(i)} \right| \times 100\% \quad (29)$$

$$E_{rms} = \frac{\sqrt{\frac{1}{M} \sum_{i=1}^{M} \left[\hat{T}(i) - T(i)\right]^2}}{T_{ave}} \times 100\% \quad (30)$$

where $T(i)$ and $\hat{T}(i)$ denote the temperature values of the i-th (i=1, 2, $\cdots$, M) node in the temperature field model and reconstructed temperature field model, and M is equal to 32 and 109 in this paper, respectively. T_{ave} represents the mean temperature of the temperature field model and can be obtained by computing the double integral divided by the area of the measured region. The regularization parameter μ controls the weight of measurement data and prior information in the solution. According to (22), since $\sigma_i > 0$ and $\mu > 0$, there is $\sigma_i + \mu/\sigma_i \geq \sigma_i$. When the value of μ is too small, $\sigma_i + \mu/\sigma_i$ will approximate σ_i, which cannot effectively suppress noise interference. However, when the value of μ is too large, $\sigma_i + \mu/\sigma_i$ will deviate greatly from σ_i, which will lead to a low confidence of the solution for the measurement data, and the solution will be too smooth and lose too much detail information. Much research has been conducted on how to select an appropriate regularization parameter, and some methods have been developed. In most cases, the parameter is selected by experience. In this paper, let μ be equal to 5×10^{-4}, and the standard Tikhonov regularization is directly used to find the slowness value of nodes. Though the method may introduce large reconstruction errors, it can be used as a simple way to verify the correctness of the algorithm. Since the system of equations is underdetermined, a least-squares solution of the equations will be obtained. The corresponding errors for the three temperature fields are presented in Tables 1, 2, and 3, respectively.

TABLE 1. Reconstruction errors of unimodal symmetry model.

Cell models	E_{max} (%)	E_{mean} (%)	E_{rms} (%)
3-node triangle	39.15	14.51	18.31
4-node square	8.85	2.61	3.18
6-node triangle	※	※	※

As listed in these tables, all the errors of the 3-node model are larger than those of the 4-node model. The main reason is that the shape function of the 4-node model uses quadratic terms in x and y, and the function approximation is better. For the 6-node model, the ※ in the table indicates that

TABLE 2. Reconstruction errors of unimodal skew model.

Cell models	E_{max} (%)	E_{mean} (%)	E_{rms} (%)
3-node triangle	40.64	14.72	18.18
4-node square	10.83	3.60	4.33
6-node triangle	※	※	※

TABLE 3. Reconstruction errors of bimodal skew model.

Cell models	E_{max} (%)	E_{mean} (%)	E_{rms} (%)
3-node triangle	41.26	14.31	19.53
4-node square	13.68	5.06	7.61
6-node triangle	※	※	※

the correct solution cannot be obtained and thus the error cannot be calculated. The main reason is that the system of equations is severely underdetermined, with 24 equations solved for 109 unknowns, which is impossible without any available prior information. Another study also shows the case of solving underdetermined equations: 24 equations with 100 unknowns were solved using SVD with an error of less than five percent, which is acceptable. Both cases are severely underdetermined, where the former is unsolvable and the latter is solvable, and the reason needs to be investigated. After calculating the condition number of the coefficient matrix, it is found that the condition number of the former is extremely smaller, about ten, while that of the latter is larger than 10^4. The larger the condition number, the more ill-conditioned the matrix, and the more susceptible the solution of the system of equations to tiny changes in the measurement data, and vice versa. The coefficient matrix of the latter is constructed based on radial basis functions, and the condition number is usually large. Meanwhile, the coefficient matrix of the former is constructed based on a piecewise polynomial approximation with a minimal condition number. That is, the mathematical principles for constructing the coefficient matrix are different, which leads to different condition numbers. The condition number is the main difference between the two matrices, but it is not sufficient to explain why the former is not solvable while the latter is. This paper believes that the main reason is that the latter uses prior information about the temperature field and the temperature distribution and the chosen basis function are similar in shape. Only in this case can the system of equations be solved and satisfactory results be obtained when the system of equations is severely underdetermined. Studies have focused on how to select basis functions that are closer to the shape of the temperature field distribution [20], [21]. The more similar the shape, the better the function approximation. Since the 3-node model has large errors and the 6-node model cannot be solved, only the reconstructed temperature field corresponding to the 4-node model is presented here. The slowness value corresponding to 32 nodes is calculated, the corresponding temperature value can be obtained following (1), and then the
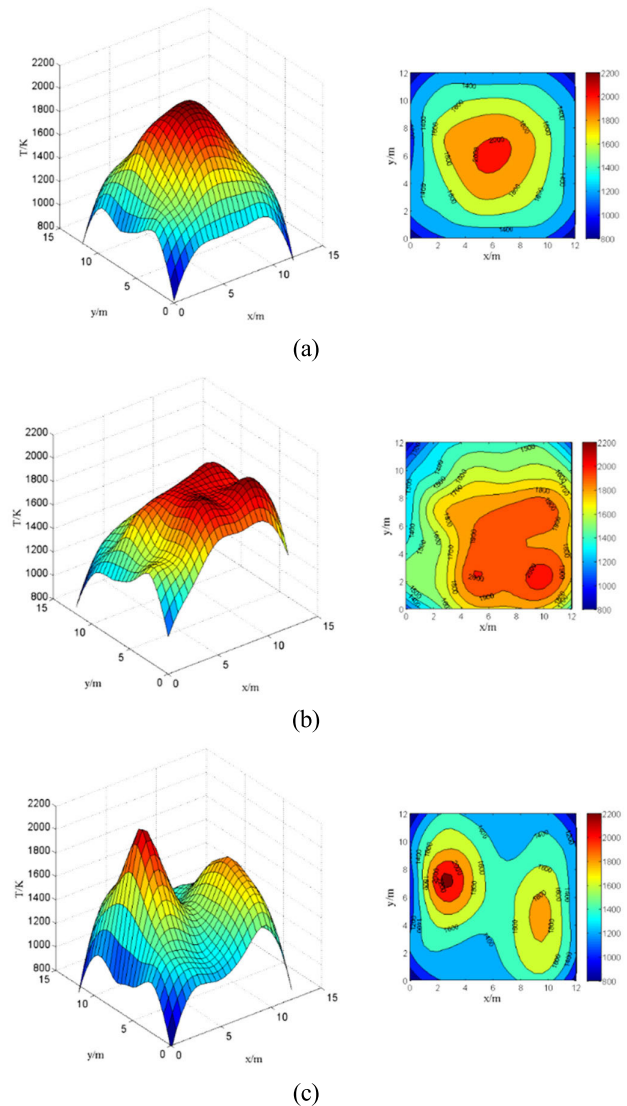

FIGURE 6. Reconstruction of the temperature field. (a) unimodal symmetry. (b) unimodal skew. (c) bimodal skew.

reconstructed temperature field can be obtained by using the interpolation method, as illustrated in Figure 6.

As illustrated in Figure 6, the reconstructed and original temperature fields are considerably different, especially at the four corner positions. The reason for this is as follows:

a) The underdetermined system of equations leads to large errors in the temperature values, and naturally, the temperature field interpolated using these data has a large error.

b) 32 pieces of original data are too few, resulting in low reconstruction accuracy.

c) Since nodes with four corners are not used, the temperature fields of the four corners are calculated by extrapolation, and the error is large. To address the above issues, the following measures are taken:

a) The number of transducers is increased to 16 so that the number of effective sound rays is increased from 24 to 96, thereby alleviating the problem of underdetermined equations.

b) The amount of original data is increased by using the 6-node model. Since the area occupied by the four corners is about four percent of the entire temperature field, they can be ignored. By discarding 12 nodes in the four corners, the number of unknowns is reduced from 121 to 109, and the dimension of the system of equations becomes 96×109. As a result, higher reconstruction accuracy is achieved. Finally, the improved layout is illustrated in Figure 7. After the optimization of the placement of the transducers, the acoustic ray does not pass through the four triangular meshes at the corners.
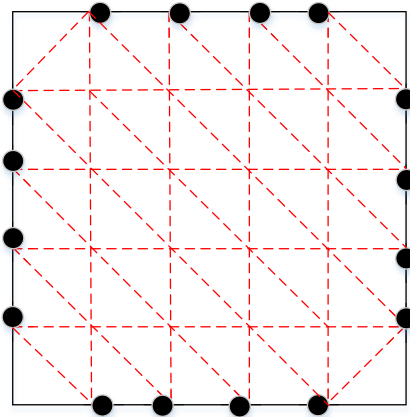

FIGURE 7. 96×109 improved layout.

By using the improved Tikhonov regularization method in Section IV and setting the threshold constant $k = 10^{-3}$, Table 4 shows the errors of the three temperature field models. The corresponding reconstructed temperature field is presented in Figure 8.

TABLE 4. Three types of temperature field reconstruction errors.

Temperature model	E_{max} (%)	E_{mean} (%)	E_{rms} (%)
Unimodal symmetry	2.94	0.59	0.69
Unimodal skew	3.25	0.69	0.87
Bimodal skew	3.68	1.09	1.28

All reconstruction errors were found to be small and acceptable. It is easy to understand that the more complex the temperature field, the larger the error. Meanwhile, the reconstructed temperature field matches the original extremely well, except for the four-corner region.

C. THE COMPARISON WITH RECONSTRUCTION METHOD BASED ON RADIAL BASIS FUNCTION AND SVD

The classical temperature field reconstruction algorithm based on the least square method is simple in principle and performs well in practice. However, due to the strict restriction that the number of grid divisions in the measured region cannot exceed the number of effective acoustic propagation
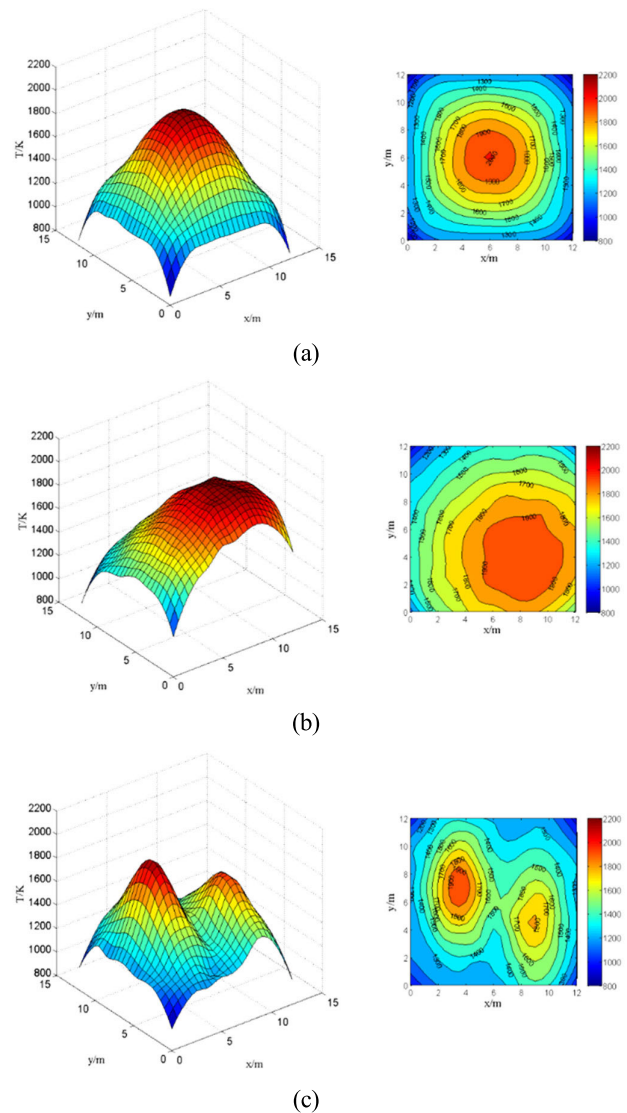

(a)

(b)

(c)

FIGURE 8. Reconstruction of the temperature field by using the 96×109 layout. (a) unimodal symmetry. (b) unimodal skew. (c) bimodal skew.

paths (i.e., the corresponding linear equations $Ax=b$ must be overdetermined equations), the reconstructed results have low accuracy. Meanwhile, due to the use of an interpolation method to reconstruct the temperature field, there will be serious temperature information loss at the boundary of the measured area. In this section, considering the excellent ability of the radial basis function (RBF) in function approximation and fitting to scattered and sparse data, along with the advantage of SVD in handling ill-conditioned problems, they are taken to compare with the proposed reconstruction method.

The RBF takes spatial distance as its unique variable, and it can approximate almost any function. RBF has the advantages of less computation and high fitting accuracy. Attributed to its strong ability to fit dispersed data, it has been widely used in physics and other fields. Common RBFs include

Gaussian (GS) function, Markov (MK) function, Multiquadric (MQ) function, inverse multiquadric (IMQ) function, and thin plate spline (TPS) function. Wang et al. [25] employed the logarithmic-quadratic (LQ) RBF and SVD method to reconstruct the complex temperature field in the boiler furnace with less measured data. The LQ function has good range, smoothness and sensitivity to parameters and overcomes the defects of other classical RBFs, so it is more suitable for fitting dispersed and complex temperature data. Reconstruction methods based on LQ RBF and SVD are used and compared with the proposed method. The temperature field model in Figure 5 was reconstructed with the layout in Figure 7. The corresponding reconstructed temperature field is demonstrated in Figure 9. The errors of the three temperature field models are listed in Table 5.

TABLE 5. Temperature field reconstruction errors of lq brf and svd-based method.

Temperature model	E_{max} (%)	E_{mean} (%)	E_{rms} (%)
Unimodal symmetry	2.47	0.78	0.78
Unimodal skew	2.56	0.72	0.95
Bimodal skew	3.15	1.11	1.38

By comparing various errors and reconstruction temperature fields, the following conclusions are made. The proposed method has a greater maximum error than the LQ RBF method, and the other two methods perform slightly better than the LQ RBF method. The maximum error appears in the four-corner region, and this is consistent with the previous observation. Since the LQ RBF method has better global approximation ability, the reconstructed temperature field is closer to the temperature field model overall. However, the local region of the temperature field is not very smooth and has more burrs. To sum up, the proposed method has higher reconstruction accuracy.

VI. EXPERIMENTAL TESTING AND ANALYSIS
To better verify the proposed reconstruction method and prove its universality, an experimental data-based verification was conducted. An experimental platform was built, and the TOF acquisition circuit was designed. To generate driving acoustic signals with high stability and strong anti-interference, the ultrasonic driving circuit must have strong output power. To obtain weak echo signals with noise, the echo-receiving circuit should have strong amplification ability and filtering ability. Additionally, the onset time of the output acoustic wave and the arrival time of the echo are important parameters for calculating the TOF, so the ultrasonic driving circuit should be designed to transmit synchronous pulses, and the ultrasonic receiving circuit should be matched with the corresponding data acquisition system to acquire echo signal waveforms and send them to the host computer for analysis. Through a comprehensive anal-
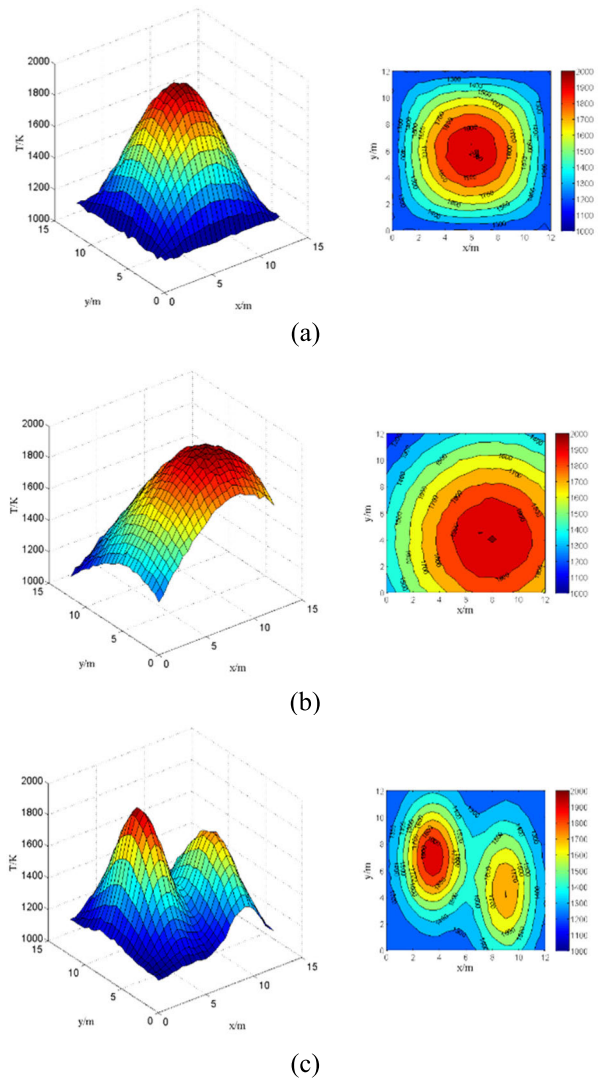

(a)

(b)

(c)

FIGURE 9. Reconstruction of the temperature field by LQ RBF and SVD. (a) unimodal symmetry. (b) unimodal skew. (c) bimodal skew.
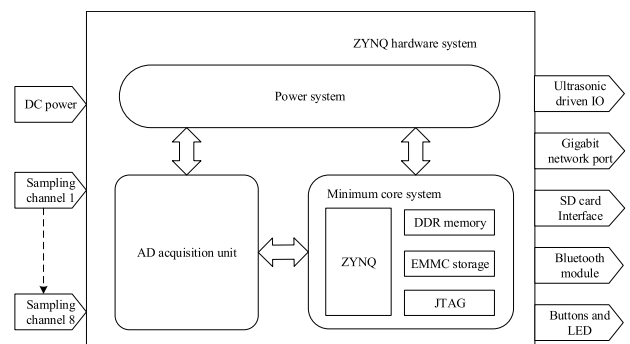

FIGURE 10. ZYNQ hardware system.

ysis of the software and hardware functional requirements of the temperature measurement system, this paper selects the ZYNQ system, an FPGA+ARM heterogeneous system, as shown in Figure 10.

A. EXPERIMENT SYSTEM

To reconstruct the two-dimensional temperature field, the system needs to design the ultrasonic driving sequence and should be able to perform multi-channel echo signal acquisition. Meanwhile, the signal generation and signal acquisition of this system are designed around ZYNQ to realize various functions. The ZYNQ system is an embedded heterogeneous system promoted by Xilinx Corporation in recent years. The hardware system of ZYNQ is mainly composed of a minimum core system, a power supply system, an AD acquisition system, a transmission control system, etc.

Its most important feature is the integration of FPGA and ARM cores. It not only supports the flexible design of the digital logic through the FPGA part and parallelized data acquisition but also uploads streaming data to the host computer by using the Gigabit Ethernet protocol supported by the ARM core. Considering the multi-channel transceiver signal acquisition and control requirements of the system, using the ZYNQ chip as the core control unit of the embedded system is an excellent way to set up the ultrasonic temperature measurement system. This paper designed the baseboard around the ZYNQ core system, and the ultrasonic drive circuit, multi-channel echo acquisition circuit, power supply circuit, data upload, and local storage interface based on Gigabit Ethernet and SDIO protocol are integrated into the baseboard. The final hardware PCB is presented in Figure 11, and the physical object is shown in Figure 12.
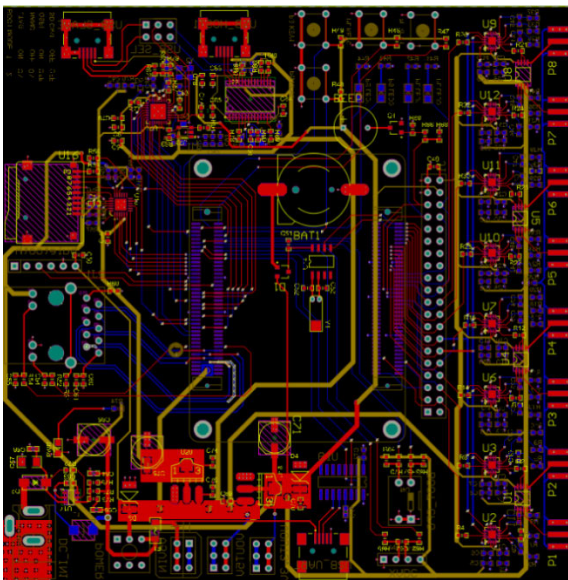

FIGURE 11. PCB design.

A long-distance (3-10m) array ultrasonic layout is completed according to the design requirements of the temperature field size. The selected ultrasonic transceivers need to have a beam range as narrow as possible and a driving voltage as high as possible. Additionally, the higher the ultrasonic frequency, the higher the frame refresh rate, but the stronger the attenuation effect. Therefore, it is necessary to balance
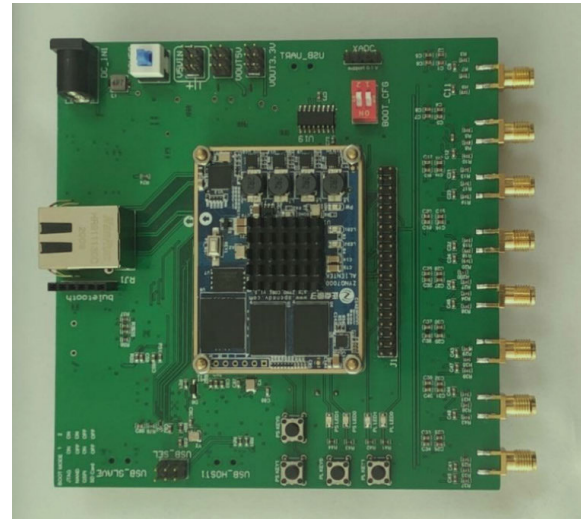

FIGURE 12. Physical object.

the frame refresh rate and attenuation intensity to select an appropriate driving frequency. The frequency of high temperature turbulence noise is concentrated below 10 KHz. Thus, to mitigate the interference of noise on the useful signal, the frequency of driving sound waves is at least 20 KHz. Finally, the system selected a center frequency of 40 KHz, the farthest theoretical transmission distance of 16 m, and the highest driving voltage of 18 V for ultrasonic transceivers to complete the design. The key parameters of ultrasonic transceivers are listed in Table 6.

TABLE 6. Key parameters of ultrasonic transceivers.

Center frequency	Emission sound pressure level	Beam angle	Supply voltage
40 ± 1 KHz	≥ 110 dB	$75 \pm 10°$	5V~18 V

A nine-sided frame with a side length of one meter was built. Nine ultrasonic transducers were used, each fixed at the vertex of the frame. The actual test environment is demonstrated in Figure 13. The operation of the system is introduced as follows: one transducer transmits the ultrasonic signal, and six transducers receive the echo signal. Then, the next transducer emits the ultrasonic signal, corresponding to six transducers receiving the echo signal, and this process continues until all transducers have emitted an ultrasonic signal. This paper uses the finite element method to divide the measured area, as shown in Figure 14. The central region is formed by isosceles right triangles, and the surrounding region is formed by irregular triangles and quadrilaterals. Meanwhile, both 6- and 4-node cell models are used. Though there are irregular triangles and quadrilaterals, this does not affect the use of the finite element method. To complete the calculation, only the coordinates of each node need to be known.
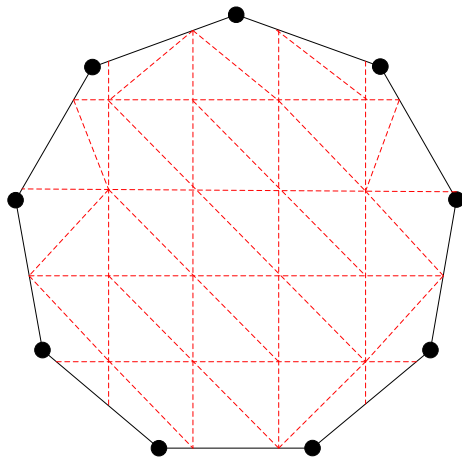
FIGURE 13. Test environment.

FIGURE 14. Finite element division of the measured area.

B. EXPERIMENT RESULTS

Unimodal symmetric and skewed temperature fields are constructed by placing the electric stove in the center and the lower right corner of the measured area, respectively. Meanwhile, two identical heat sources are placed at coordinates $(-0.75, 0)$ and $(0.75, 0)$ to form a bimodal symmetric temperature field. Figure 15 shows the reconstructed temperature field. Errors can be calculated by using the temperature values of several points in the temperature field measured by the thermocouple as the actual values and the reconstructed temperature field. The errors are listed in Table 7.

TABLE 7. Temperature field reconstruction errors of Experiment test.

Temperature model	E_{max} (%)	E_{mean} (%)	E_{rms} (%)
Unimodal symmetry	4.64	2.19	2.69
Unimodal skew	4.88	2.39	2.88
Bimodal symmetry	4.96	2.67	3.12

As shown in Figure 15, there are multiple hot spots, which is consistent with the actual situation. The ambient
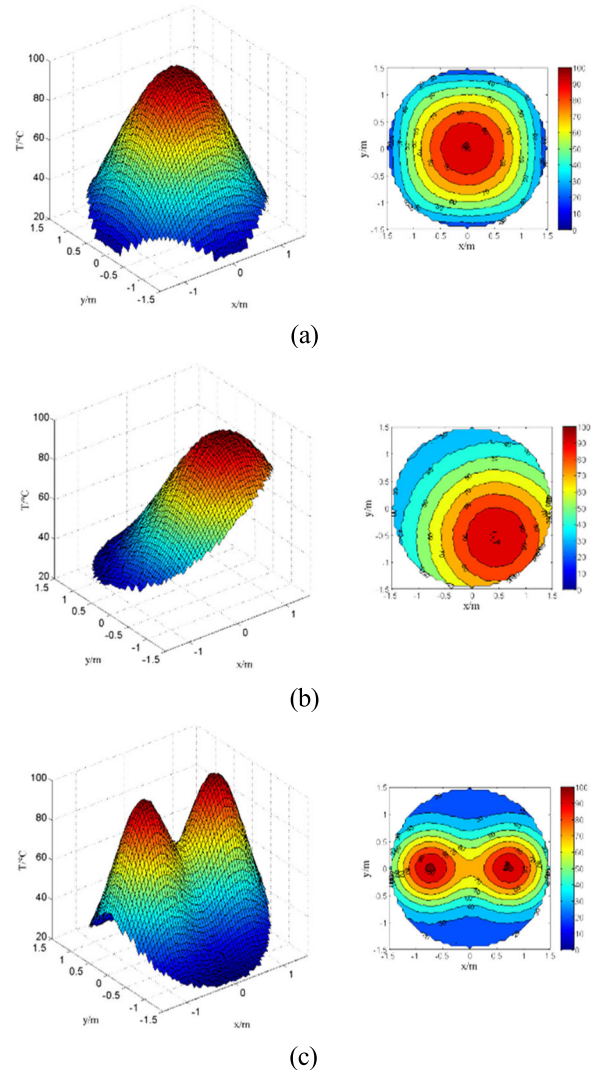

FIGURE 15. Reconstruction of the temperature field by experiment test. (a) unimodal symmetry. (b) unimodal skew. (c) bimodal symmetry.

temperature is about 25 °C, the maximum temperature of the temperature field is about 98 °C, and the reconstructed temperature value basically falls within this range. Thus, the temperature field generated by the electric stove is well reconstructed.

VII. CONCLUSION

For the reconstruction of the temperature field by acoustic tomography, it is essential to improve the reconstruction accuracy of reconstruction algorithms. In this paper, the forward problem is modeled based on finite element interpolation, and the inverse problem is solved with SVD-based regularization. Then, the distribution of the temperature field is obtained by interpolation, and three typical temperature fields are investigated quantitatively and qualitatively.

Simulation results indicate that the proposed reconstruction method is feasible with satisfactory accuracy, thus providing an alternative method for reconstructing the ultrasound

temperature field. Based on the theoretical and experimental results, the following conclusions are obtained:

1) The first step of reconstructing the ultrasound temperature field is to discretize the problem. The choice of discretization method is critical and directly affects the reconstruction accuracy of the temperature field. To the best of our knowledge, there are three main discretization methods. Classical discretization methods have large errors and can be used in situations where the reconstruction accuracy is not significant. Methods based on radial basis functions are widely adopted. Such methods have excellent global approximation capability because the shape of the basis function and the distribution of the temperature field are similar. There has been much research around finding basis functions with better approximation capabilities. Our proposed method provides polynomial piecewise approximation. It has better local approximation capability and is an alternative scheme.

2) The three discussed methods have varying computational complexity of the coefficient matrix. The radial basis function- based method requires only one integration operation to solve the coefficient matrix and is simple and easy to implement. The classical discretization method needs to find the distance traversed by the acoustic rays of each grid, and its computational demand increases with the number of rays and grids. Our proposed method, which requires piecewise integration followed by summation, is the most cumbersome but has higher accuracy. In the method, all coefficient matrices are computed offline and do not affect the real-time performance of the reconstructed temperature field.

3) The solution to the inverse problem is a crucial part of the reconstruction of the ultrasound temperature field. Mainstream methods include regularization methods based on radial basis functions, SVD, and various optimization methods. For the former, the choice of the regularization parameter and threshold constant directly affects the reconstruction results. This will be investigated in our future work.

ACKNOWLEDGMENT

REFERENCES

[1] H. Zhang, Y. Guo, and L. Wang, "Transducers layout optimization for acoustic tomography temperature field reconstruction," *IEEE Trans. Ultrason., Ferroelectr., Freq. Control*, vol. 69, no. 4, pp. 1497–1507, Apr. 2022.

[2] Q. Kong, G. Jiang, Y. Liu, and M. Yu, "Numerical and experimental study on temperature field reconstruction based on acoustic tomography," *Appl. Thermal Eng.*, vol. 170, Apr. 2020, Art. no. 114720.

[3] I. Jovanović, L. Sbaiz, and M. Vetterli, "Acoustic tomography for scalar and vector fields: Theory and application to temperature and wind estimation," *J. Atmos. Ocean. Technol.*, vol. 26, no. 8, pp. 1475–1492, Aug. 2009.

[4] M. Bramanti, E. A. Salerno, A. Tonazzini, S. Pasini, and A. Gray, "An acoustic pyrometer system for tomographic thermal imaging in power plant boilers," *IEEE Trans. Instrum. Meas.*, vol. 45, no. 1, pp. 159–167, Feb. 1996.

[5] X. Zhou, C. Dong, C. Zhao, and X. Bai, "Temperature-field reconstruction algorithm based on reflected sigmoidal radial basis function and QR decomposition," *Appl. Thermal Eng.*, vol. 171, May 2020, Art. no. 114987.

[6] S. Liu, S. Liu, and T. Ren, "Acoustic tomography reconstruction method for the temperature distribution measurement," *IEEE Trans. Instrum. Meas.*, vol. 66, no. 8, pp. 1936–1945, Aug. 2017.

[7] S. Kolouri, M. R. Azimi-Sadjadi, and A. Ziemann, "A statistical-based approach for acoustic tomography of the atmosphere," *J. Acoust. Soc. Amer.*, vol. 135, no. 1, pp. 104–114, Jan. 2014.

[8] H. Li, H. Terada, and A. Yamada, "Real-time monitoring system of vortex wind field using coded acoustic wave signals between parallel array elements," *Jpn. J. Appl. Phys.*, vol. 53, no. 7S, Jul. 2014, Art. no. 07KC18.

[9] J. Zhang, H. Qi, Y. Ji, Y. Ren, M. He, M. Su, and X. Cai, "Nonlinear acoustic tomography for measuring the temperature and velocity fields by using the covariance matrix adaptation evolution strategy algorithm," *IEEE Trans. Instrum. Meas.*, vol. 71, pp. 1–14, 2022.

[10] Z.-T. Niu, H. Qi, Z.-Y. Zhu, K.-F. Li, Y.-T. Ren, and M.-J. He, "A novel parametric level set method coupled with Tikhonov regularization for tomographic laser absorption reconstruction," *Appl. Thermal Eng.*, vol. 201, Jan. 2022, Art. no. 117819.

[11] Z.-T. Niu, H. Qi, Y.-K. Ji, S. Wen, Y.-T. Ren, and M.-J. He, "Real-time reconstruction of thermal boundary condition of porous media via temperature sequence," *Int. J. Thermal Sci.*, vol. 177, Jul. 2022, Art. no. 107570.

[12] Q. Kong, Y. Lu, G. Jiang, and Y. Liu, "Acoustic measurement of velocity filed using improved radial basic function neural network," *Int. J. Heat Mass Transf.*, vol. 202, Mar. 2023, Art. no. 123733.

[13] L. Zhang and J. Li, "Acoustic tomography temperature reconstruction based on virtual observation and residual network," *IEEE Sensors J.*, vol. 22, no. 17, pp. 17054–17064, Sep. 2022.

[14] F.-S. Lin, S. Pal, C.-Y. Lu, S.-W. Du, M.-C. Huang, C.-H. Wu, J.-L. Lin, C.-Y. Li, H.-C. Lin, and C.-H. Huang, "Reconstructing 2-D gas temperature distribution with deep neural networks," *IEEE Sensors J.*, vol. 23, no. 3, pp. 2891–2899, Feb. 2023.

[15] W. Wu, Y. Wang, Q. Liu, G. Wang, and J. Zhang, "Wavelet-improved score-based generative model for medical imaging," *IEEE Trans. Med. Imag.*, vol. 43, no. 3, pp. 966–979, Mar. 2024.

[16] X. Guo, Y. Li, D. Chang, P. He, P. Feng, H. Yu, and W. Wu, "Spectral2Spectral: Image-spectral similarity assisted deep spectral CT reconstruction without reference," *IEEE Trans. Comput. Imag.*, vol. 9, pp. 1031–1042, 2023.

[17] W. Wu, X. Guo, Y. Chen, S. Wang, and J. Chen, "Deep embedding-attention-refinement for sparse-view CT reconstruction," *IEEE Trans. Instrum. Meas.*, vol. 72, pp. 1–11, 2023.

[18] R. Jia, Q. Xiong, G. Xu, K. Wang, and S. Liang, "A method for two-dimensional temperature field distribution reconstruction," *Appl. Thermal Eng.*, vol. 111, pp. 961–967, Jan. 2017.

[19] S. Liu, S. Liu, and T. Ren, "Ultrasonic tomography based temperature distribution measurement method," *Measurement*, vol. 94, pp. 671–679, Dec. 2016.

[20] J. Zhang, H. Qi, D. Jiang, M. He, Y. Ren, M. Su, and X. Cai, "Acoustic tomography of two dimensional velocity field by using meshless radial basis function and modified Tikhonov regularization method," *Measurement*, vol. 175, Apr. 2021, Art. no. 109107.

[21] P. C. Hansen, "REGULARIZATION TOOLS: A MATLAB package for analysis and solution of discrete ill-posed problems," *Numer. Algorithms*, vol. 6, no. 1, pp. 1–35, Mar. 1994.

[22] Y. Huang and Z. Jia, "Some results on the regularization of LSQR for large-scale discrete ill-posed problems," *Sci. China Math.*, vol. 60, no. 4, pp. 701–718, Apr. 2017.

[23] Y. Yu, Q. Xiong, Q. Li, C. Wu, K. Wang, M. Gao, and S. Liang, "A method for ultrasound thermal image distribution reconstruction," *Meas. Sci. Technol.*, vol. 30, no. 9, Sep. 2019, Art. no. 095007.

[24] S. Liu, S. Liu, and G. Tong, "Reconstruction method for inversion problems in an acoustic tomography based temperature distribution measurement," *Meas. Sci. Technol.*, vol. 28, no. 11, Nov. 2017, Art. no. 115005.

[25] H. Wang, X. Zhou, Q. Yang, J. Chen, C. Dong, and L. Zhao, "A reconstruction method of boiler furnace temperature distribution based on acoustic measurement," *IEEE Trans. Instrum. Meas.*, vol. 70, pp. 1–13, 2021.

[26] H. Yan, Z. Ma, and Y. G. Zhou, "Acoustic tomography system for online monitoring of temperature fields," *IET Sci., Meas. Technol.*, vol. 11, no. 5, pp. 623–630, Aug. 2017.

[27] Q. Kong, G. Jiang, Y. Liu, and J. Sun, "3D high-quality temperature-field reconstruction method in furnace based on acoustic tomography," *Appl. Thermal Eng.*, vol. 179, Oct. 2020, Art. no. 115693.

[28] S. P. Zhang, G. Q. Shen, L. S. An, and Y. G. Niu, "Online monitoring of the two-dimensional temperature field in a boiler furnace based on acoustic computed tomography," *Appl. Thermal Eng.*, vol. 75, pp. 958–966, Nov. 2015.

[29] L. Zhao, X. Zhou, C. Dong, Y. Wu, and H. Wang, "Ultrasonic thermometry algorithm based on inverse quadratic function," *IEEE Trans. Ultrason., Ferroelectr., Freq. Control*, vol. 68, no. 5, pp. 1876–1884, May 2021.

[30] H. Yan, G. Chen, Y. Zhou, and L. Liu, "Primary study of temperature distribution measurement in stored grain based on acoustic tomography," *Experim. Thermal Fluid Sci.*, vol. 42, pp. 55–63, Oct. 2012.

[31] Y. Yu, Q. Xiong, M. Yang, C. Wu, Q. Zhu, K. Wang, and M. Gao, "Krylov subspace methods for regularized models in acoustic temperature reconstruction from simulated and real measurements," *IEEE Trans. Instrum. Meas.*, vol. 70, pp. 1–11, 2021.

[32] Y. Bao and J. B. Jia, "Nonlinear temperature field reconstruction using acoustic tomography," in *Proc. IEEE Int. Conf. Imag. Syst. Techn. (IST)*, Oct. 2017, pp. 272–277.

QIANG LI received the B.Eng. and M.Sc. degrees from the North University of China, Taiyuan, China, in 2019 and 2022, respectively. His current research interests include measuring the temperature field using acoustic travel-time tomography and electronic circuit design.

HAITAO ZHANG received the B.Eng. degree (Hons.) from the Tianjin Institute of Technology, Tianjin, China, in 2003, and the M.Sc. degree (Hons.) from Shanxi University, Taiyuan, China, in 2008. He is currently pursuing the Ph.D. degree with the National Key Laboratory of Information Detection and Processing, North University of China. His current research interests include measuring the temperature field using acoustic travel-time tomography.

LIMING WANG received the Ph.D. degree in measuring and testing technologies and in instruments from the North University of China, Taiyuan, China, in 2005. He is currently a Professor with the Department of Information and Communication Engineering, North University of China. His research interests include electromagnetic detection techniques and non-destructive testing.

• • •